



## Research article

# Black phosphorus-based nanoparticles induce liver cancer cell mitochondrial apoptosis and immune cell tumor infiltration for enhancing dendritic cell therapy

Ke Liao<sup>a,b</sup>, Shang Chen<sup>a,b,d</sup>, Gun Yang<sup>a,b</sup>, Xin Huang<sup>b,e</sup>, Tianyuan Wang<sup>b</sup>, Shoubin Long<sup>b</sup>, Jing Wang<sup>b</sup>, Lei Yin<sup>b</sup>, Qingshuang Zou<sup>c</sup>, Quan Liu<sup>b,f</sup>, Zifen Guo<sup>a,\*</sup>

<sup>a</sup> Institute of Pharmacy and Pharmacology, School of Pharmaceutical Science, Hengyang Medical School, University of South China, Hengyang, Hunan, 421001, PR China

<sup>b</sup> Department of Laboratory Medicine, Huazhong University of Science and Technology Union Shenzhen Hospital (Nanshan Hospital), Shenzhen University, Shenzhen, 518052, PR China

<sup>c</sup> Department of Chemistry, The Chinese University of Hong Kong, Shatin, N.T., Hong Kong, PR China

<sup>d</sup> Guangdong Key Laboratory for Biomedical Measurements and Ultrasound Imaging, National-Regional Key Technology Engineering Laboratory for Medical Ultrasound, School of Biomedical Engineering, Shenzhen University Medical School, Shenzhen, 518060, PR China

<sup>e</sup> Department of Thoracic Surgery, First Affiliated Hospital of Anhui Medical University, Hefei, 230032, PR China

<sup>f</sup> Division of Hepatobiliary and Pancreas Surgery, Department of General Surgery, Shenzhen People's Hospital (The Second Clinical Medical College, Jinan University), Shenzhen, 518020, PR China

## ARTICLE INFO

## Keywords:

Liver cancer  
Photothermal therapy  
Dendritic cells  
Black phosphorus  
Tertiary lymphatic structures

## ABSTRACT

Cellular immunotherapy is a crucial aspect of current tumor immunotherapy, though it presents several challenges such as immune cell dysfunction, limited recognition of neoantigens, and inadequate lymphocyte infiltration into the tumor microenvironment. This study proposes a novel approach utilizing a combination of dendritic cell (DC)-based cellular immunotherapy and a photothermal nanoadjuvant black phosphorus (BP) nanoparticles to overcome these challenges. A new platform called PLGA@BP-R848, which consists of modifying poly-(lactic-co-glycolic acid) (PLGA) onto BP nanosheets loading the immune adjuvant R848. The PLGA@BP-R848 nanoparticles demonstrated exceptional drug delivery and release capabilities, as well as a photothermal effect, biocompatibility, and the ability to activate the mitochondrial apoptotic pathway Bcl-2-Bax-Cytochrome c-caspase-3 and inhibit the PI3K-AKT-mTOR signaling pathway. In a hepatocellular carcinoma mouse model, the binding of PLGA@BP-R848 nanoparticles and dendritic cells primed with GPC3 peptides, successfully induced a systemic anti-tumor immune response. PLGA@BP-R848 nanoparticles bolster immune cell infiltration into tumors and induce cancer cell apoptosis. The synergistic therapy involving dendritic cells and photothermal nanoadjuvant effectively suppressed tumor growth, and facilitated the formation of tertiary lymphatic structures (TLS) in tumors. This study presents a novel approach in using photothermal nanoadjuvants to advance antitumor effect of cellular immunotherapy, such as DCs therapy.

\* Corresponding author.

E-mail address: [guozifen76@163.com](mailto:guozifen76@163.com) (Z. Guo).

<https://doi.org/10.1016/j.heliyon.2024.e27234>

Received 25 January 2024; Received in revised form 23 February 2024; Accepted 26 February 2024

Available online 2 March 2024

2405-8440/© 2024 The Authors. Published by Elsevier Ltd. This is an open access article under the CC BY-NC-ND license (<http://creativecommons.org/licenses/by-nc-nd/4.0/>).

## 1. Introduction

The main challenges in the immunotherapy of solid tumors are the dysfunction of immune cells, the insufficient recognition of neoantigens, and a lack of infiltrating lymphocytes in the tumor [1,2]. However, the anti-tumor effects of tumor immune cell therapy in immunologically cold solid tumors are often weakened by physical barriers and immunosuppressive tumor microenvironment (TME) [3]. Currently, tumor immunotherapy encompasses a solitary therapeutic strategy that incorporates immune checkpoint inhibitors alongside immune cell therapy. While these treatments demonstrate considerable therapeutic efficacy in specific instances, they also present certain challenges. Immune checkpoint inhibitors, such as PD-1 and CTLA-4, may encounter resistance and display limited therapeutic efficacy in certain patients, which may potentially give rise to immune-related adverse events like immune-mediated pneumonia and hepatitis [4,5]. However, despite the notable therapeutic efficacy of cell therapy in select hematologic malignancies, its use in solid tumor treatment encounters obstacles prominently including immune tolerance. Additionally, CAR-T cell therapy induces cytokine storms, leading to an irreversible damage to the body [6]. Consequently, to overcome these deficiencies, several strategies have been utilized, including surgery, radiation/chemotherapy, nanomedicines, and combination therapies with checkpoint inhibitors [7]. Multifunctional nanomaterials have recently exhibited immense promise in the realms of drug release and antigen delivery systems. Drug release can be controlled to achieve a sustained release in the body, reduce drug toxicity, and improve therapeutic efficacy by creating specific surface properties, particle size, and structure of nanomaterials [8]. Additionally, they can serve as carriers for antigens and immune adjuvants to enhance immune cell recognition and activation of antigens, thereby enhancing immune responses. Multifunctional nanomaterials are photothermal conversion agents able to destroy tumor cells through photothermal effects, alter TME, activate immune cells, and enhance the killing of tumor cells by immune cells [9]. Therefore, the combination strategy using a multifunctional nanoplatform has aroused extensive interest in cancer immunotherapy. Recently, a multifunctional nanoplatform for PTT combined with STING agonists was developed using polydopamine loaded with the STING agonists and  $Mn^{2+}$ , which synergistically triggers a powerful immune response by facilitating the smart release of the drugs and inducing immunogenic cell death through photothermal effects [10]. In addition, there is growing evidence of the importance of multifunctional nanoplatforms capable of combining different clinical drugs for specific biomedical applications, delaying further disease progression and future clinical applications [11,12].

Light-nano-immunoadjuvant combined with DC/CAR-T cell immunotherapy is a promising synergistic cancer treatment thanks to its non-invasiveness, low systemic toxicity, excellent laser controllability, and effective tumor antigen exposure through photodynamic ablation, thereby activating the anti-tumor immunity of the body. However, the effectiveness of photodynamic therapy is limited by low singlet oxygen ( $^1O_2$ ) production and aggregation-induced quenching caused by conventional photosensitizers, which attenuated the impact at the site of the tumor [13]. Another frequently employed photothermal therapy (PTT) involves the accumulation of agents responsive to near-infrared light (NIR) in the tumor, wherein the light is converted into thermal energy to destroy tumor cells upon exposure to laser radiation [14]. This suggests the possibility to generate anti-tumor immune responses by generating tumor-specific antigens from the remaining ablated tumor cells. However, PTT may superheat the target region within a certain range, with the risk of involving and damaging normal tissues [15].

Black phosphorus (BP) has garnered attention as a prominent inorganic 2D nanomaterial owing to its numerous novel attributes. These comprise a notable NIR extinction coefficient, exceptional photothermal conversion efficiency, impressive surface-to-volume ratio, substantial drug loading capacity, good biocompatibility and biodegradability, as well as producing non-toxic phosphates

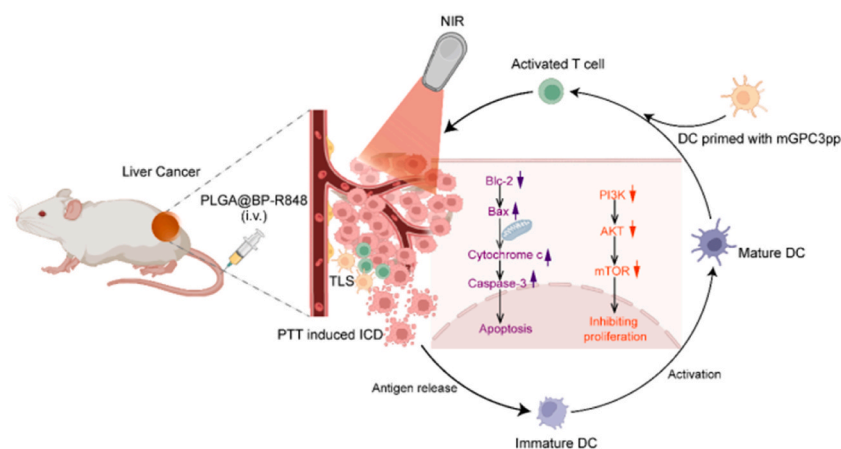


**Fig. 1.** Graphic illustration shows the structure of PLGA@BP-R848 NPs and its application in cancer immunotherapy. PLGA@BP-R848 NPs constructed by PLGA, BP, and R848, are introduced into tumor tissues and exposed to 808 nm NIR laser irradiation. Upon generating photothermal effects, these PLGA@BP-R848 NPs initiate the mitochondrial apoptotic signaling pathway (Bcl-2-Bax-Cytochrome c-caspase-3), thereby hindering the PI3K-AKT-mTOR signaling pathway responsible for cell growth regulation. The ICD induced by PLGA@BP-R848 NPs stimulates the maturation of dendritic cells (DCs), activates T cells, and promotes the formation of tertiary lymphoid structures (TLS). Furthermore, the combination of DCs primed with mGPC3pp enhances the efficacy of cancer immunotherapy.

and phosphoric esters as ultimate degradation products [16]. This provides a natural advantage for the delivery and exposure of tumor antigens and immunoadjuvants using nanomaterials. For example, Li Z et al. achieved efficient loading of the anti-tumor drug adriamycin and effective elimination of tumors by exploiting the multi-fold structure of BP NSs as well as their good photothermal properties [17]. Furthermore, a low dosage of BP facilitates dendritic cells (DCs) maturation and stimulate natural killer (NK) cells [18]. Furthermore, BP-induced localized PTT triggers immunogenic cell death (ICD), stimulates DC maturation, increases tumor tissue blood flow and vascular permeability, and alters stromal pressure, thereby promoting T cell infiltration in solid tumors [19]. BP was encapsulated into PLGA to reduce its toxicity due to its toxic effect at high doses. High-dose BP exerts therapeutic effects after photothermal irradiation by inducing toxic damage [20]. Resiquimod (R848) is an agonist of toll-like receptors 7 and 8, which stimulates DC maturation, reshapes the immunosuppressive TME, and induces inflammatory responses [21]. Therefore, the combination of BP nanoparticles (NPs) and R848 not only has high potential when used in phototherapy and drug delivery but it represents great promise for the development and clinical application in the treatment of tumors *in vivo*.

This work describes a therapeutic strategy combining cell immunotherapy with BP nanosheets loaded with R848. Biodegradable BP nanosheets possess high NIR extinction coefficient and were chosen as PTT agents to convert laser energy into heat. R848 were used to generate immune adjuvant effects. The obtained PLGA@BP-R848 NPs were irradiated with pulsed laser, which induced PTT that generated heat to ablate the tumor. This process resulted in cellular apoptosis and the eradication of primary tumors, while minimizing any potential side effects. Crucially, the administration of PTT with R848-loaded NPs resulted in the production of tumor-related antigens. In response, these additives elicited potent immune responses against tumors. The generated immune response, when combined with DC immunotherapy, was subsequently augmented and effectively inhibited residual tumor growth. This resulted in the formation of tertiary lymphatic structures (TLS), thereby strengthens the local anti-tumor immune response and suppressing tumor growth. Fig. 1 illustrates the overall therapeutic strategy of combining PLGA@BP-R848 NPs with immune cell therapy.

## 2. Materials and methods

### 2.1. Materials

The BP powder (purity  $\geq 99.99\%$ ) was procured from Shanxi Ruixi Company. Mitochondrial membrane potential assay kit with JC-1 and Calcein AM/PI was obtained from Biotime Ltd. R848 was purchased from Solarbio Ltd. Antibodies against Bcl2, Bax, Caspase-3, Cytochrome c,  $\beta$ -actin and PI3K-AKT-mTOR signaling pathway were acquired from Cell Signaling Technology (USA).

### 2.2. Synthesis of PLGA@BP-R848 NPs

Firstly, we homogeneously dispersed 20 mg of black phosphorus (BP) powder in 30 ml of isopropyl alcohol. The probe was then sonicated in ice water for 6 h (3 s on/off cycle) to prevent thermal oxidation. Next, we transferred the suspension to an ultrasonic water bath and continued sonication for about 10 h at 4 °C. After sonication, we centrifuged the mixture at 3000 rpm for 30 min and then centrifuged the supernatant again at 8500 rpm for 30 min. We then dried the centrifuged BP NPs precipitate under vacuum and stored it away from light. Subsequently, We resuspended the dried BP nanoparticles in PLGA at a 1:1 ratio and homogenized them evenly using ultrasonication. Subsequently, 1 mg of R848 and 20  $\mu$ L of PLGA solution were added sequentially under stirring. Finally, the pH was adjusted by adding NaOH solution aqueous (10 mg/mL, 20 $\mu$ l). The solution was stirred for 4 h under light protection, then centrifuged at 12,000 rpm to collect the precipitate. Which was then washed.

### 2.3. Characterization of PLGA@BP-R848 NPs

The size and zeta potential were determined using a Nano Zetasizer analyzer. The elemental composition, morphology, and structure of the nanomaterials were examined using an FEI Tecnai G2 F30 TEM instrument and a JEOL JSM-7800F scanning electron microscope. Chemicals on the surface of PLGA@BP-R848 NPs were analyzed using a XPS instrument with Al K $\alpha$  radiation ( $\lambda = 0.83$  nm,  $h\nu = 1486.7$  eV). The morphology and height of the PLGA@BP-R848 NPs were examined using a Bruker Dimension FastScan. UV-Vis absorption spectra were recorded using a Hitachi UH4150 spectrophotometer for PLGA@BP-R848 NPs in the 100–200 nm range.

### 2.4. Cytotoxicity of PLGA@BP-R848 *in vitro*

LO2, Hepa1-6, and HepG2 cells (ATCC) were cultured in DMEM supplemented with FBS (10%; Gibco) and penicillin/streptomycin (1%; Gibco). All cells were grown at 37 °C in a carbon dioxide environment with 5% CO<sub>2</sub>. Cells ( $1 \times 10^5$ ) were seeded into 96-well plates and after overnight incubation, different concentrations of PLGA@BP-R848 NPs diluted in the medium for 24 h. Subsequently, it was assayed with Cell Counting Kit-8.

### 2.5. Cell uptake of PLGA@BP-R848 NPs

HepG2 cells were seeded into a 12-well plate at a density of  $1 \times 10^5$  cells/well. After allowing for cell attachment, Cy5.5-labeled PLGA@BP-R848 NPs (1 mg/mL, 100  $\mu$ L, n = 3) were introduced to the wells for co-culturing. 2–4 h later, the cells were treated with Hoechst (Invitrogen, cat. no. 66249) and phalloidin (Beyotime, cat. no. C1033) before being examined with an Olympus FV3000.

## 2.6. Extraction of BM-DCs

Three C57BL/6 mice were euthanized, and their bodies were soaked in 75% alcohol. The hind legs were removed, and the muscles and tissues were carefully dissected while maintaining sterility. Bone marrow cells were collected, gently dispersed, and then filtered through a cell filter (Corning, cat. no. 352350). Red blood cell lysate was applied on ice for 10 min to lyse any remaining red blood cells. Afterward, the harvested cells were cultured in complete DMEM medium supplemented with GM-CSF (20 ng/mL, PeproTech) and IL-4 (20 ng/mL, PeproTech) for 5 days in 10 cm plates. Murine-derived GPC3 peptides (mGPC3pp, 10 µg/ml) were then added, and the cells were further cultured for 3 days. The BM-DCs were stained with CD11c-APC antibody (BD), CD80-FITC antibody (BD), and CD86-PerCP-Cy7 antibody (BD). Flow cytometry (BD FACS Calibur) was utilized to assess the purity of BM-DC maturation.

## 2.7. *In vitro* photothermal effect of PLGA@BP-R848

HepG2 cells were inoculated into 96-well plates at a density of  $1 \times 10^5$  cells/well ( $n = 4$ ) and incubated overnight. Subsequently, the cells were treated with various concentrations of PLGA@BP-R848 NPs in DMEM medium. After 8 h of cultivation, an 808 nm laser (1.0 W/cm<sup>2</sup>, 8 min) was used to irradiate each well. The CCK-8 assay was utilized to evaluate the relative cell viability at a wavelength of 450 nm after 12 h. The photothermal effect of PLGA@BP-R848 NPs under 808 nm laser illumination was studied. To do this, samples at various concentrations were placed in a transparent quartz plate and exposed to 808 nm laser (1 W/cm<sup>2</sup>) for 8 min. Temperature change and photothermal stability of PLGA@BP-R848 nanoparticles were monitored. This was accomplished by subjecting the samples to 808 nm laser irradiation (1 W/cm<sup>2</sup>) for 8 min, followed by cooling to room temperature. This process was duplicated five times. The influence of environmental factors on the stability of BP and PLGA@BP-R848 NPs was established by dispersing both in water. Their photothermal efficacy was documented after incubation for different time periods, when they were placed to 808 nm laser exposure for 8 min.

## 2.8. The toxicity of PLGA@BP-R848 *in vivo*

C57BL/6 mice (Female, 6–8 weeks old) were procured from Beijing Vital River Laboratory Animal Technology Co., Ltd. Rearing under SPF conditions. C57BL/6 mice were randomised into three groups ( $n = 24$ ) and injected with PLGA@BP (1 mg/ml, 100 µL), PLGA@BP-R848 (1 mg/ml, 100 µL) and PBS via tail vein, respectively. blood and major organs (heart, liver, spleen, lungs and kidneys) were collected from each group on days 1, 7 and 28 to assess the *in vivo* toxicity of nanoparticles.

## 2.9. *In vivo* biodistribution of PLGA@BP-R848

Hepa1-6 cells were injected into the buttocks of Balb/c rats. When the tumour volume reached 150 mm<sup>3</sup>, they've divided into two groups and tail vein injected with Cy5.5-labeled PLGA@BP-R848 (1 mg/mL, 100 µL;  $n = 6$ ) or PBS. The imaging system (IVIS Spectrum CT, PerkinElmer, USA) detected the fluorescence signal at 8 h and 12 h after injection. At these time points, the main organs (heart, liver, spleen, lung, and kidney) as well as the tumors were dissected to detect fluorescent signals.

## 2.10. *In vivo* anticancer evaluation

BALB/c mice (Female) carrying subcutaneous Hepa1-6 hepatocellular carcinoma tumors were used as the animal model. The mice ( $n = 6$ ) were randomly divided into five groups: (1) control, (2) PLGA@BP, (3) PLGA@BP-R848, (4) PLGA@BP + 808 nm laser, (5) PLGA@BP-R848 + 808 nm laser. PLGA@BP and PLGA@BP-R848 (10 mg/kg, 100 µL) were administered by intravenous injection for 2 times at day 1 and day 7. Then, In the laser groups, the tumor site was exposed to an 808 nm laser (1 W/cm<sup>2</sup>, 8 min) after 24 h of injection. We monitored the tumor size and body weight every two days, calculating the tumor volume using the formula:  $V = (\text{length}) \times (\text{width})^2 / 2$ . The tumor of all groups was dissected after 15 days and submerged in 4% formalin, then, embedded in paraffin for immunohistology staining of Ki67, CD31, CA9, CD4, CD8 and H&E staining. Spleen cells obtained from all groups were also stained with anti-CD8 and anti-CD4 antibodies to evaluate the outcomes of immunotherapy.

## 2.11. Evaluation of synergistic antitumor *in vivo*

C57BL/6 mice (female) were injected subcutaneously with Hepa1-6 cells ( $5 \times 10^6$ , 75 µL) in the right buttock to establish a mouse subcutaneous hepatocellular carcinoma model. When the tumor volume reached approximately 100 mm<sup>3</sup>, the mice ( $n = 5$ ) were randomly assigned to four groups: (1) control group (saline, 100 µL), (2) DCmGPC3pp (1 mg/ml, 100 µL), (3) PLGA@BP-R848+NIR (1 mg/ml, 100 µL), (4) PLGA@BP-R848-DCmGPC3pp + NIR (1 mg/ml, 100 µL). After 24 h, photothermal therapy was administered (808 nm, 1 W/cm<sup>2</sup>, 8 min). The same treatment procedure was repeated on day 7 after the previous hyperthermia treatment. Tumor volume was measured at one day intervals for a total of 18 days using a digital caliper. All mice were sacrificed at the end of the 18-day period. Remove tumors from each group of mice to study the immune cells within the tumour, and they were homogenized to create a single cell suspension following the instructions (Tumor Dissociation Kit, Miltenyi, cat. no. 130-096-730). CD3<sup>+</sup>CD8<sup>+</sup>IFN-γ and CD3<sup>+</sup>CD4<sup>+</sup>IFN-γ were used to stain CTLs and effector helper T cells, respectively. For analyzing CD4<sup>+</sup> effector helper T cells, cells in the secondary tumor were stained with anti-CD3-FITC (Biolegend), anti-CD4-PE (Biolegend), and anti-IFN-γ-APC (Biolegend) antibodies following a standard protocol. Likewise, to analyze CTLs, cells in the secondary tumor were stained with anti-CD3-FITC

(Biolegend), anti-CD8-PE (Biolegend), and anti-IFN- $\gamma$ -APC (Biolegend) antibodies. Immunosuppressive Tregs in the secondary tumor were also further stained with anti-CD4-FITC (Biolegend), anti-CD25-PE (Biolegend), and anti-Foxp3-APC (Biolegend) antibodies.

### 3. Results

#### 3.1. Preparation and characterization of PLGA@BP-R848 NPs

The PLGA@BP-R848 NPs were synthesized using BP NPs and R848, modified with PLGA. The BP NPs were obtained using the ultrasonic stripping method, building upon our previous research [22]. The structure characterization of PLGA@BP and PLGA@BP-R848 NPs was conducted through the utilization of transmission electron microscopy (TEM) (Figure S1 and Fig. 2A). The surface morphology and thickness of the PLGA@BP-R848 NPs can be observed in the atomic force microscopy (AFM) image, and the thickness measured by the cross-sectional analysis ranged from 1 to 3 nm (Fig. 2B). Fig. 2C shows that BP with a diameter of 148.4 nm was obtained. BP NPs were modified with PLGA to enhance their dispersion through electrostatic force, leading to an increase in particle size to approximately 162.6 nm. The Raman peak of PLGA@BP-R848 NPs in Fig. 2D shows the three peaks of Ag1, B2g and Ag2. The chemical composition of PLGA@BP-R848 NPs was determined by XPS (Fig. 2D), which shows a calibrated binding energy of 133.9 eV for various elements, the C1s peak was recorded. In the P2p spectrum, the presence of zero-valence P was indicated by two doublets at 130.2 eV and 129.3 eV, corresponding to P2p1/2 and P2p3/2, respectively. Fig. 2E shows STEM with energy dispersive

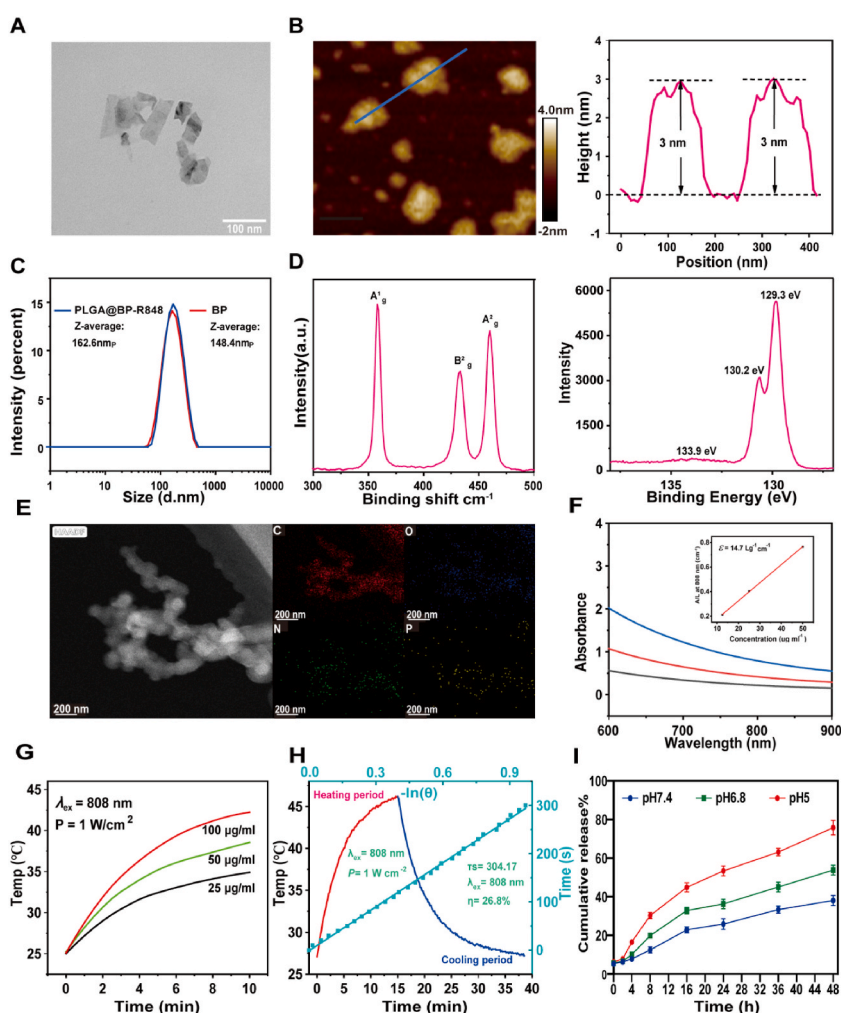


**Fig. 2.** Preparation and characterization of PLGA@BP-R848 NPs. A. Transmission electron microscopy (TEM) images of PLGA@BP-R848 NPs (scale bar = 100 nm). B. AFM image of PLGA@BP-R848 NPs and the corresponding thickness (scale bar = 10 nm). C. XPS spectrum of PLGA@BP-R848 NPs. D. Raman scattering spectrum of PLGA@BP-R848 NPs. E. FTIR spectra of PLGA@BP-R848 NPs. F. UV-Vis-NIR absorption spectra ( $\lambda = 808$  nm) of different concentrations of PLGA@BP-R848 dispersions. G. Heating curves of different concentrations of PLGA@BP-R848 dispersions irradiated by 808 nm laser ( $1 \text{ W/cm}^2$ ). H. Photo-thermal conversion efficient in PLGA@BP-R848 NPs. I. Drug release curves of PLGA@BP-R848 NPs at different pH values.

X-ray spectroscopy mapping of PLGA@BP-R848 NPs showing the co-localization of N, C, O, and P elements. The UV absorbance intensity of BP, PLGA@BP and PLGA@BP-R848 NPs under NIR laser irradiation is shown in Fig. 2F. The photothermal stability of PLGA@BP-R848 NPs, superior to BP NPs, showed consistent effects across heating cycles (Fig. S2). Fig. 2G provided a diagrammatic representation of the drug loading and activation mechanism of PLGA@BP-R848 NPs. The release triggered by light was examined by observing changes in the UV–vis absorption spectra under physiological conditions. Once the R848 was loaded on BP NPs, it was released only under NIR irradiation. The photothermal-conversion efficiency of PLGA@BP-R848 NPs at 808 nm was 26.8%, consistent with a previous study (Fig. 2H). There existed ample evidence indicating the inherent acidity of the TME or lysosomes. Taking into consideration the release profile of R848 by PLGA@BP-R848 NPs in acidic environments, we monitored drug release spectra of PLGA@BP-R848 NPs at pH 5.0 (acidic), pH 6.8 (weakly acidic), and pH 7.4 (neutral) *in vitro* using the absorbance value at 425 nm. The results showed a continuous increase and cumulative release reaching its maximum within the first 48 h. The cumulative release of R848 was more effective in acidic medium compared to weakly acidic and neutral mediums, as shown in Fig. 2I. These results indicated that PLGA@BP-R848 NPs effectively released adjuvants by NIR irradiation in stimulated TME or lysosomes. Therefore, PLGA@BP-R848 NPs achieved intelligent controlled release of adjuvants, reduced the toxic side effects of drugs in the body, and improved therapeutic effectiveness.

### 3.2. The biocompatibility, photothermal capabilities, and tumor-targeting performance of PLGA@BP-R848 NPs

The *in vitro* photothermal effects, cytotoxicity and biocompatibility of PLGA@BP-R848 NPs were experimentally evaluated. Human hepatocellular cancer cells LO2, murine hepatocellular cancer cells Hepa 1–6, and human hepatocellular cancer cells HepG2 were treated with various concentrations of PLGA@BP-R848 nanoparticles for 24 h. Both PLGA@BP and PLGA@BP-R848 NPs did not exert any cytotoxicity (Fig. 3A and B). Then, the photothermal efficacy of PLGA@BP and PLGA@BP-R848 NPs at varying concentrations (0, 25, 50, and 100  $\mu\text{g}/\text{ml}$ ) was evaluated in HepG2 cells. The results illustrated a concentration-dependent enhancement of the photothermal killing effect across various nanoparticles (Fig. 3C–D). Additionally, HepG2 cells were processed with PLGA@BP-R848 NPs for 4 h to visualize NPs uptake and localization. Fluorescent images showed that HepG2 cells underwent apoptosis (red markers) with increasing concentration due to localized PTT induced by PLGA@BP-R848 NPs (Fig. 3E). The intracellular delivery of PLGA@BP-R848 NPs was efficiently promoted, indicating the enhanced uptake by endocytosis of Cy5.5-labeled PLGA@BP-R848 NPs, which were

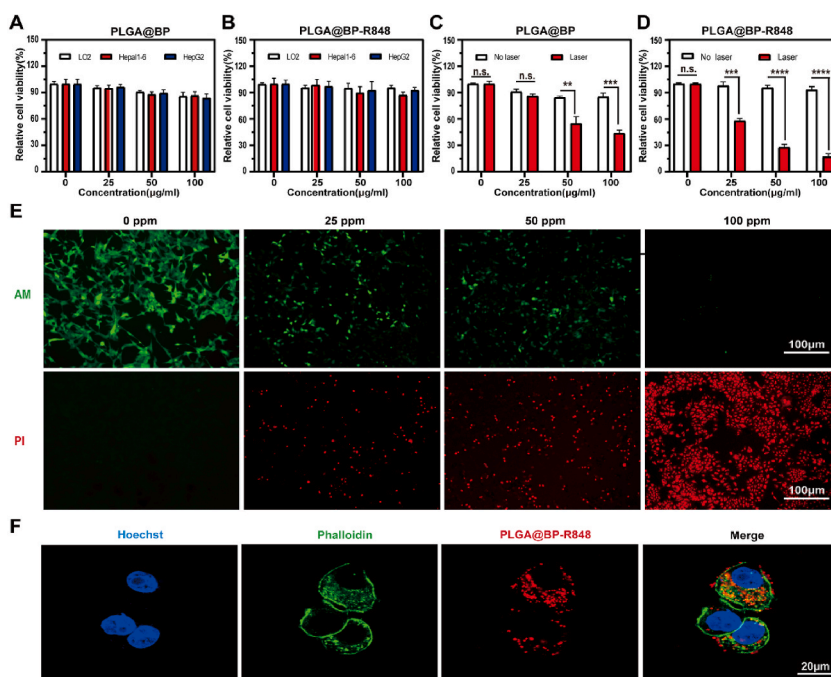


**Fig. 3. Biocompatibility, photothermal performance, cytotoxicity *in vitro* and *in vivo* biodistribution of PLGA@BP-R848 NPs.** A and B. Relative viability of LO2, Hepa 1–6, and HepG2 cells after incubation with BP and PLGA@BP-R848 NPs at various concentrations (0, 25, 50, and 100  $\mu\text{g}/\text{ml}$ ). C and D. Relative survival of HepG2 cells after culture with BP and PLGA@BP-R848 NPs at various concentrations (0, 25, 50, and 100  $\mu\text{g}/\text{ml}$ ) and photothermal ablation without and with laser power (1  $\text{W}/\text{cm}^2$ , 8 min). (\* indicates  $p < 0.05$ , \*\* indicates  $p < 0.01$ , \*\*\* indicates  $p < 0.001$ , \*\*\*\* indicates  $p < 0.0001$ , and n.s. indicates no significant difference). E. Fluorescence imaging of HepG2 cells induced by PLGA@BP-R848 NPs at various concentrations (0, 25, 50, and 100  $\mu\text{g}/\text{ml}$ ) and photothermal ablation, stained with calcein-AM (green for live cells) and propidium iodide (red for dead cells). Scale bar = 100  $\mu\text{m}$ . F. Confocal images of the uptake of PLGA@BP-R848 NPs by HepG2 cells (blue: cell nucleus; green: lysosome stained; red: Cy5.5-labeled PLGA@BP-R848), scale bar = 20  $\mu\text{m}$ . (For interpretation of the references to colour in this figure legend, the reader is referred to the Web version of this article.)

successfully internalized by HepG2 cells (Fig. 3F).

Subsequently, the toxicity of PLGA@BP-R848 NPs was further investigated *in vivo*. The C57BL/6 mice were randomised into two groups: (1) control group, which was administered an intravenous injection of saline, (2) PLGA@BP-R848 NPs group, which was administered an intravenous injection of PLGA@BP-R848 NPs at dose of 5 mg/kg BP per mouse. On day 1, 7, and 28 after injection, blood samples from mice were assessed, along with histological examination of major organs such as lung, liver, spleen, kidney, and heart. Hematological parameters such as RBC (red blood cells), WBC (white blood cells), HCT (hematocrit), HB (hemoglobin), MCH (mean corpuscular hemoglobin), MCHC (mean corpuscular hemoglobin concentration), MCV (mean corpuscular volume), and PLT (platelets) were measured in order to establish reference ranges. No hematotoxicity was detected in the group treated with PLGA@BP-R848 NPs group at days 1, 7 and 28 (Fig. S3). In addition, the liver and kidney functions were assessed through the measurement of standard blood biochemical parameters including ALB (albumin), ALT (alanine transaminase), AST (aspartate transaminase), (TP) total protein, CrEnz (creatinine enzyme), and UREA (urea). The analysis of these parameters showed no significant abnormalities between groups of mice (Fig. S3). Furthermore, the main organs stained with H&E on day 1, day 7, and day 28 showed no obvious pathological toxicity (Fig. S4). These results suggest that PLGA@BP-R848 NPs possess very good biocompatibility.

Cy5.5-labeled PLGA@BP-R848 NPs were injected via tail vein into Balb/c nude mice carrying tumors, and the nanomaterials were observed by fluorescence imaging to have different levels of aggregation of the nanomaterials their *in vivo* in both the organs and the tumors after 8h and 12h (Fig. 4A–B). Tumor frozen section examination revealed the presence of Cy5.5 fluorescence in the tumor at 8 h and 12 h post-injection, indicating the accumulation of PLGA@BP-R848 NPs at the tumor site (Fig. S5). In addition, the photothermal effect of PLGA@BP-R848 NPs on passive tumor targeting was assessed using an imaging system. Fig. 4B shows that both BP and PLGA@BP-R848 exerted an effective photothermal effect dependent on NIR exposure time. Following a 5-min irradiation, the mouse tumour site temperature rises from about 34 °C to over 40 °C, with the temperature increase in the PLGA@BP-R848 group (44.9 °C) being higher than that in the BP alone group (41.7 °C), while the temperature increase in the PBS group was minimal (Fig. 4C–D). This result indicated that PLGA@BP-R848 had a synergistic photothermal effect compared to the BP alone *in vivo*, thus being more conducive on inducing ICD and accelerating tumor cell rupture. Collectively, these findings demonstrated the significant biocompatibility, photothermal effect and tumor-targeting capability of PLGA@BP-R848 NPs in facilitating the photo-triggered ablation of cancer cells.

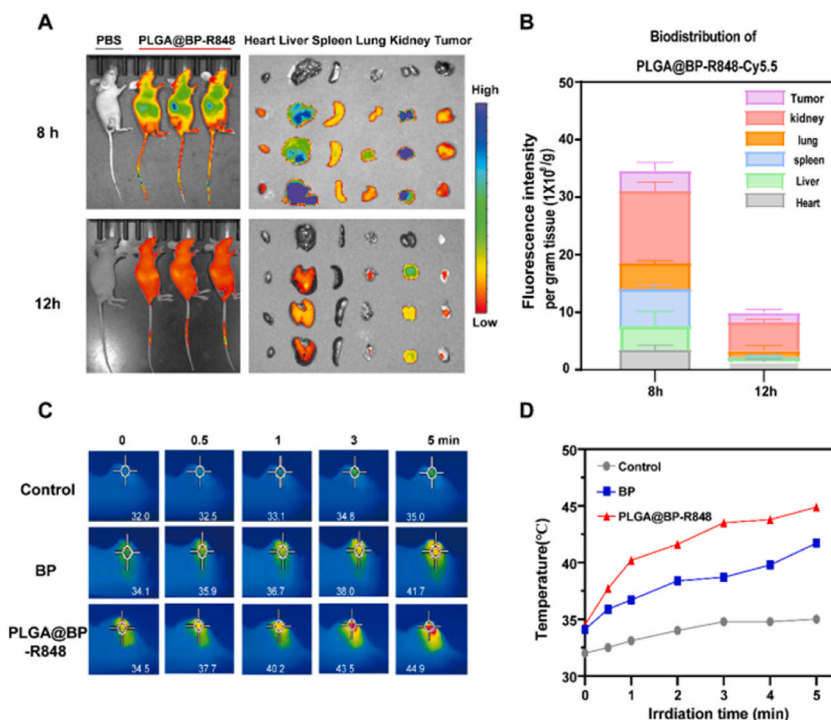


**Fig. 4.** *In vivo* tumor targeting and distribution of Cy5.5-labeled PLGA@BP-R848 NPs. A. Fluorescence images of the tumor and organs at 8 and 12 h after injecting Cy5.5-labeled PLGA@BP-R848 NPs. B. Quantitative distribution analysis of Cy5.5-labeled PLGA@BP-R848 NPs in nude mice based on the average fluorescence. C. Thermal maps and the increase in temperature over time in Hepa1-6 tumor-bearing mice exposed to an 808 nm laser (1 W/cm<sup>2</sup>, 8 min) and injected saline (100  $\mu$ L), BP NPs (1 mg/mL), and PLGA@BP-R848 (1 mg/mL). D. Statistical graph of temporal changes in body temperature of mice in Figure C.

### 3.3. Potential antitumor mechanisms of PLGA@BP-R848 NPs

To investigate the potential antitumor mechanisms further, western blotting was employed to study the expression of apoptosis-related proteins. Mitochondria have a strong association with cell apoptosis [23]. HepG2 cells were exposed to various concentrations of PLGA@BP-R848 NPs (0, 25, 50, and 100  $\mu\text{g}/\text{ml}$ ) and subsequently subjected to laser irradiation at a power density of 1  $\text{W}/\text{cm}^2$  for a duration of 8 min. The mitochondrial membrane potential was evaluated using JC-1 probe solution to detect cells in early apoptosis (normal: red; damaged: green), as well as the degree of mitochondrial damage that was positively correlated with the concentration of PLGA@BP-R848 NPs. (Fig. 5A). In the mitochondrion-mediated pathway, the balance between proapoptotic factors (like Bax) and antiapoptotic factors (like Bcl-2) strictly governs cell apoptosis [24]. This balance is crucial in deciding a cell's fate—survival or apoptosis. Moreover, the Bcl-2 family influences apoptosis by releasing cytochrome C from the mitochondria to the cytosol, initiating apoptotic body formation and caspase activation [25]. After the treatment of HepG2 cells with PLGA@BP-R848 NPs for 24 h, the supernatant showed an increase in the content of cytochrome c, which was PLGA@BP-R848 NP-concentration dependent (Fig. 5B). The upregulation of Bax and the concomitant downregulation of Bcl-2 indicated that the induction of apoptosis resulting from PLGA@BP-R848 NPs treatment was more noticeable with the increase in concentration, in comparison to the control group, indicating that high concentrations of PLGA@BP-R848 NPs are superior to low concentrations in inducing intrinsic apoptosis (Fig. 5C). PLGA@BP-R848 NPs administration resulted in cytochrome c and caspase-3 upregulation compared to control (Fig. 5C), demonstrating that PLGA@BP-R848 NPs induced tumor cell death through the Bcl-2-Bax-cytochrome-c-caspase-3-associated apoptotic mechanism. The mitochondria in tumor cells underwent apoptosis induced by PLGA@BP-R848 NPs, resulting in the inhibition of tumor cell proliferation. The PI3K-AKT-mTOR signaling pathway is crucial for regulating cell proliferation and growth [26]. Our results suggested that the downregulation of PI3K-AKT-mTOR signaling pathway by high concentrations of PLGA@BP-R848 NPs was more evident than that obtained with low doses, indicating that PLGA@BP-R848 NPs were able to induce the dysregulation of PI3K-AKT-mTOR signaling pathway (Fig. 5D). These findings revealed that high PLGA@BP-R848 NPs were able to induce hepatocellular carcinoma cell apoptosis and inhibit proliferation compared with the low doses.

### 3.4. In vivo anti-tumor immune responses

In order to investigate the efficacy of PLGA@BP-R848 NPs in tumor phototherapy, *in vivo* experiments were conducted on Hepa 1–6 tumor-bearing mice, according to the results obtained *in vitro*. The mice were randomly divided into five treatment groups: (1) physiological saline, (2) PLGA@BP, (3) PLGA@BP-R848, (4) PLGA@BP + NIR (photothermal combined immunotherapy), (5) PLGA@BP-R848 + NIR (photothermal combined immunotherapy) (Fig. 6A). Each group received the first intravenous injection into the tail vein (5 mg/kg) on the second day of 50 mm tumors measured, and the group 4 and 5 underwent 8-min NIR laser irradiation

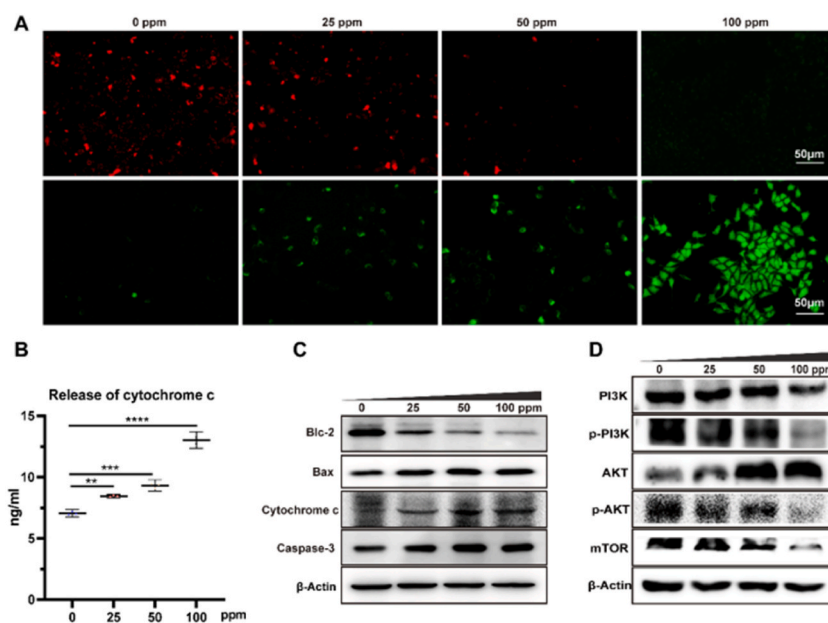


**Fig. 5.** Antitumor effects of PLGA@BP-R848 NPs. A. Fluorescence imaging of HepG2 cells incubated PLGA@BP-R848 NPs at various concentrations (0, 25, 50, and 100  $\mu\text{g}/\text{ml}$ ) stained with JC-1 (green, dead cells; red, live cells). scale bar = 100  $\mu\text{m}$ . B. Release of cytochrome c from HepG2 cells supernatant incubated at different PLGA@BP-R848 NPs concentrations for 24 h (\*\* indicates  $p < 0.01$ , \*\*\* indicates  $p < 0.001$ , \*\*\*\* indicates  $p < 0.0001$ ). C. Immunoblotting analysis for mitochondrial apoptosis-related proteins (Bcl-2, Bax, Cytochrome c, and caspase-3). D. Immunoblotting analysis for proteins related to the PI3K-AKT-mTOR signaling pathway. (For interpretation of the references to colour in this figure legend, the reader is referred to the Web version of this article.)

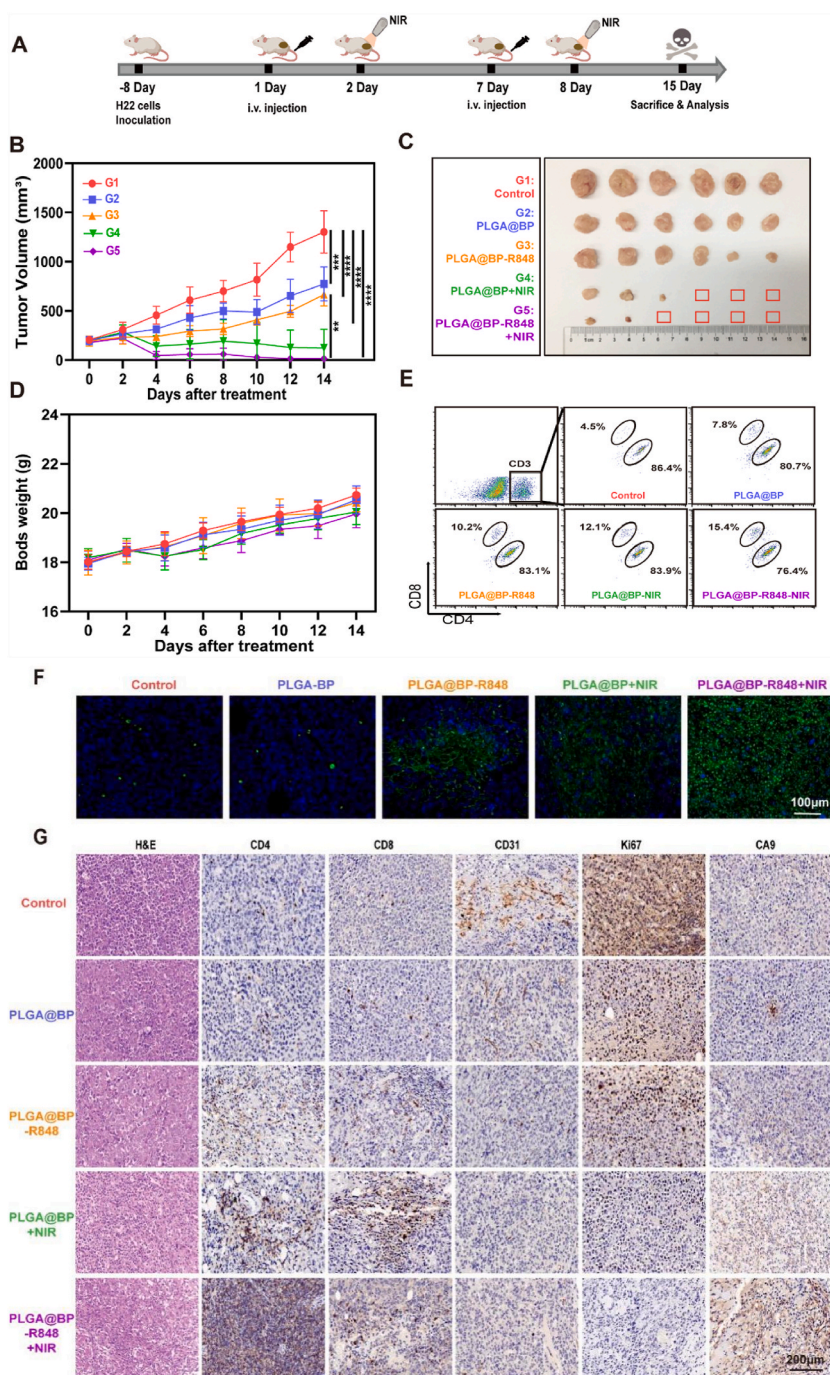


**Fig. 6.** *In vivo* therapeutic impact of PLGA@BP-R848 nanoparticles in Hepa1-6 tumor-bearing mice. A. Schematic representation of the establishment of the tumor model and the process of therapy for various treatments. B. Changes in tumor volume under different treatments. (\*\* indicates  $p < 0.01$ , \*\*\* indicates  $p < 0.001$ , and \*\*\*\* indicates  $p < 0.0001$ ). C. Picture of the tumour after 18 days of treatment. D. Changes in body weight under different group. E. Analysis of CD3<sup>+</sup>, CD4<sup>+</sup>T and CD8<sup>+</sup> T cells in the spleens of mice under different treatments using flow cytometry ( $n = 3$ /group). F. TUNEL-Hoechst co-staining assays of tumors treated with different methods. G. H&E staining, and CD4, CD8, CD31, Ki67, CA9 immunohistochemical staining for pathological changes in the tumors.

after 24 h of injection. Each group received a second intravenous tail injection on the seventh day, and the group 4 and 5 repeated the laser irradiation described above. The treatment concluded on day eighteen, at which point all mice from each group were sacrificed for analysis. We further explored the photothermal and immunotherapeutic effects of PLGA@BP-R848 NPs *in vivo*. The changes in tumor volume over time are depicted in Fig. 6B. As anticipated, the NPs-treated group exhibited a superior treatment effect compared

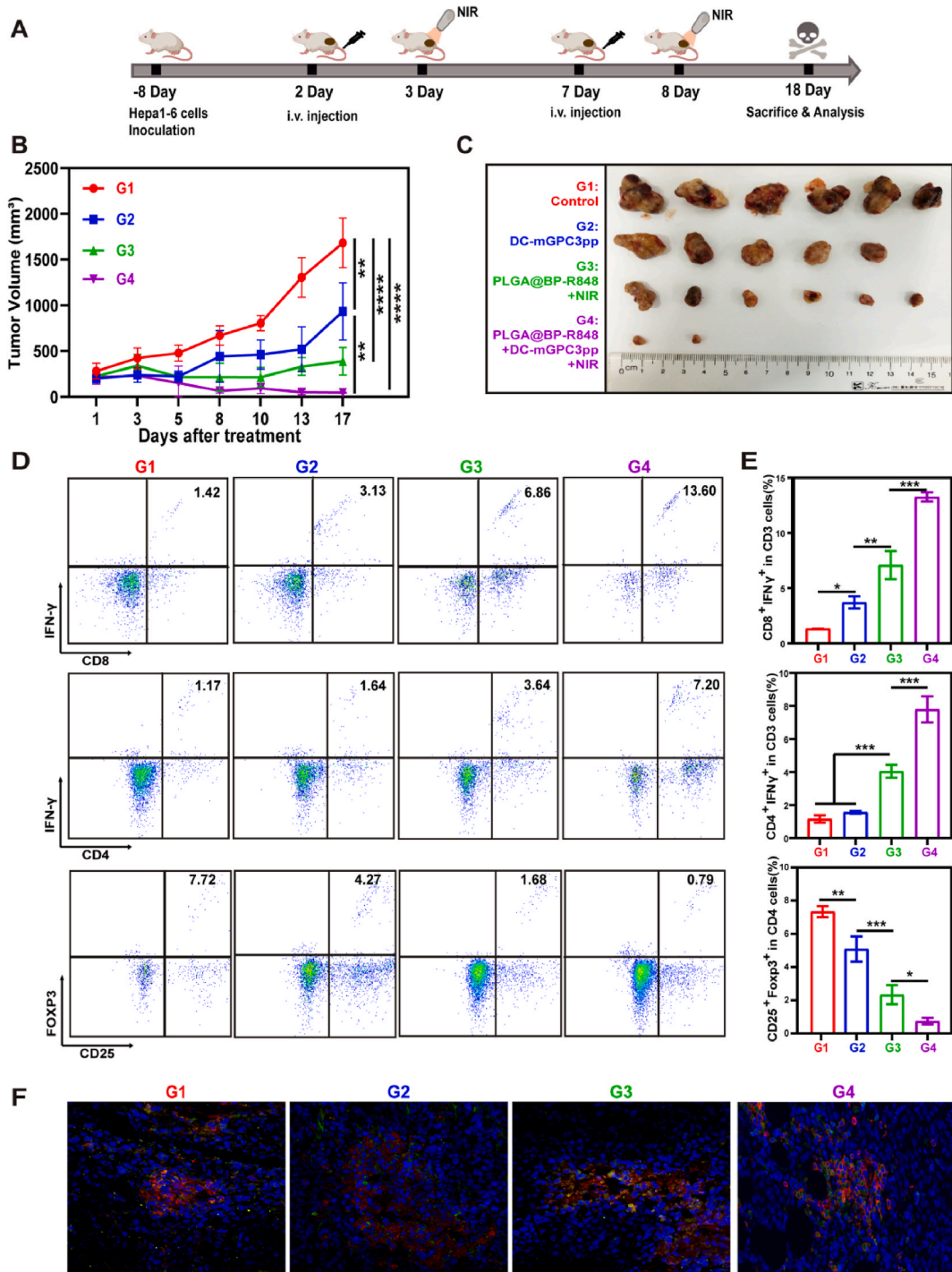


**Fig. 7.** In vivo therapeutic efficiency of PLGA@BP-R848 NPs combined with mGPC3pp-DC immune cell in Hepa1-6 cancer-bearing mice. **A.** Illustration representation of the treatment process in the tumour model. **B.** The change in tumor size with different treatments (G1, Control group; G2, DC vaccine group stimulated by GPC3 antigen peptide (DC-mGPC3pp); G3, PLGA@BP-R848 combined with NIR group; G4, PLGA@BP-R848 combined with DC-mGPC3pp and NIR phototherapy group (PLGA@BP-R848+DC-mGPC3pp + NIR)). **C.** Pictures of tumor tissues 18 days after intravenous administration of different therapies. **D.** Measurement of CD3<sup>+</sup>CD8<sup>+</sup> IFN- $\gamma$ <sup>+</sup>, CD3<sup>+</sup>CD4<sup>+</sup> IFN- $\gamma$ <sup>+</sup>, and CD4<sup>+</sup>CD25<sup>+</sup>FoxP3<sup>+</sup> T cells through flow cytometry after different treatments. **E.** Measurement of CD3<sup>+</sup>CD8<sup>+</sup>IFN- $\gamma$ <sup>+</sup>, CD3<sup>+</sup>CD4<sup>+</sup>IFN- $\gamma$ <sup>+</sup>, and CD4<sup>+</sup>CD25<sup>+</sup>FoxP3<sup>+</sup> T cells through flow cytometry after different treatments. (\* indicates  $p < 0.05$ , \*\* indicates  $p < 0.01$ , \*\*\* indicates  $p < 0.001$ , and \*\*\*\* indicates  $p < 0.0001$ ). **F.** Multiplex immunofluorescence assay of a representative TLS in various groups showing CD3<sup>+</sup> (green), CD20<sup>+</sup> (red) and DAPI (blue). (For interpretation of the references to colour in this figure legend, the reader is referred to the Web version of this article.)

to the control group. Furthermore, the group subjected to laser irradiation had smaller tumors compared to the non-irradiated group. The PLGA@BP-R848 treatment group showed inhibited tumor growth compared to both the control and PLGA@BP groups, suggesting that R848 also plays a role in affecting tumors *in vivo*. The tumor in the PLGA@BP + NIR laser group was remarkably small compared to the PLGA@BP group, likely due to the accumulated BP NPs in the tumor producing a photothermal effect that killed tumor cells (Fig. 6B–C). Day 10 after treatment, tumor growth was significantly reduced in both the PLGA@BP NPs laser groups and PLGA@BP-R848 NPs laser groups with the tumors that shrank and gradually disappeared. Notably, the anti-tumor efficacy of the PLGA@BP-R848+NIR groups surpassed that of the PLGA@BP + NIR groups. This suggests that R848 activated immune cells in a more powerfully manner to suppress tumor growth (Fig. 6B–C). The results demonstrated that the combination of PLGA@BP-R848 NPs with 808 nm laser produced a remarkable synergistic effect on the eradication of tumors and demonstrated an effective anti-tumor impact. The body weight of all mice after the 15 days of treatment did not show any noticeable reduction and kept a slight upward trend (Fig. 6D).

Next, splenocytes were incubated in RPMI-1640 medium to further explore the potential anti-tumor immune mechanisms used by PLGA@BP-R848 NPs. The levels of CD4<sup>+</sup> T cells (CD3<sup>+</sup> CD4<sup>+</sup> cells) and CD8<sup>+</sup> T cells (CD3<sup>+</sup> CD8<sup>+</sup> cells) in the spleen were determined by flow cytometry. The spleen of mice immunized with PLGA@BP-R848 under 808 nm light illumination exhibited a higher amount of CD8<sup>+</sup> T cells compared to other two groups (Fig. 6E). Additionally, the percentage of CD8<sup>+</sup> T cells in the spleen of mice immunized with PLGA@BP-R848 without NIR irradiation was significantly higher than that in the control group, indicating that PLGA@BP-R848 effectively activated the immune system *in vivo* (Fig. 6E). TUNEL staining is not affected by external laser irradiation and can accurately indicate DNA fragmentation due to cell apoptosis rather than cell necrosis [27]. In the control group, only a few apoptotic cells were observed, with intact nuclear morphology of tumor cells. A little number of apoptotic cells (green particles) was seen in the BP, PLGA@BP, and PLGA@BP-R848 groups. Most tumor cells in the PLGA@BP-R848 laser group showed dark brown nuclear particles, indicating that PLGA@BP-R848 significantly induced tumor cell apoptosis (Fig. 6F). The impact of PLGA@BP-R848-based PTT on TME was further explored to investigate whether it affected the tumor inflammatory microenvironment, including heat-induced inflammation, angiogenesis, and tumor recurrence [28]. For this purpose, the residual tumor was analyzed after treatment in each group. The number of CD4<sup>+</sup> and CD8<sup>+</sup> cells increased in the tumor after PLGA@BP-R848 PTT treatment, indicating a change in the tumor immune response within the TME (Fig. 6G). CD31<sup>+</sup> vascular dysfunction, significant reduction in Ki67<sup>+</sup> hepatocellular proliferation, and increased CA9<sup>+</sup> hypoxia signals were detected. Therefore, these results suggested that PLGA@BP-R848-based PTT induced malignant cell death and significantly altered the TME. Moreover, they indicated that abundant R848 released from PLGA@BP-R848 NPs primarily induced the differentiation of the naive T cells into cytotoxic T lymphocytes (CTLs) and helper T cells rather than regulatory T cells (Tregs), thereby enhancing immune cell infiltration into the tumor. BP produced a photothermal effect that killed cancer cells, promoted mitochondrial apoptosis in tumor cells, and prevented tumor cell proliferation and metastasis. Therefore, PLGA@BP-R848 NPs showed excellent phototherapy efficiency and performed an immunotherapy against tumors.

### 3.5. *In vivo* PLGA@BP-R848 NPs combined with mGPC3pp-DC vaccine for anti-tumor therapy

The ability of PLGA@BP-R848+NIR phototherapy in combination with mouse liver cancer GPC3 antigen peptide (mGPC3pp) DC vaccine to induce an anti-tumor immune response *in vivo* was investigated given the excellent performance of PLGA@BP-R848+NIR *in vitro* in the immune modulation and ablation of mouse liver cancer. Bone marrow-derived DCs were stimulated with mouse GPC3 antigen peptide and the maturation of the markers CD86<sup>+</sup> and CD80<sup>+</sup> in CD11c<sup>+</sup> cell population was examined by flow cytometry. The percentage CD11c<sup>+</sup> cells expressing both CD86<sup>+</sup> and CD80<sup>+</sup> was found to be over 95%, indicating the complete functionality of DCs and its ability to effectively mobilize anti-tumor immunity (Fig. S6).

In order to establish a mouse model of hepatocellular carcinoma, Hepa1-6 cells were injected into the right buttock of female C57BL/6 mice. Once the tumor volume on both sides reached 50 mm<sup>3</sup>, divided into four groups: G1, control group; G2, DC vaccine group stimulated by GPC3 antigen peptide (DC-mGPC3pp); G3, PLGA@BP-R848 combined with NIR group; G4, PLGA@BP-R848 combined with DC-mGPC3pp and NIR phototherapy group (PLGA@BP-R848+DC-mGPC3pp + NIR). The treatment plan is shown in Fig. 7A. On the second day of 50 mm tumors measured, the formulations of each group were injected into the tail vein of mice. Subsequently, the mice were exposed to NIR radiation for 8 min, 24 h after injection. A second treatment using the same procedure was carried out on day 7. The observations were continued until day 18 after the treatment (Fig. 7A). As anticipated, all groups diminished tumor proliferation compared to the G1 group (Fig. 7B). The treatment efficacy of PLGA@BP-R848+NIR group and PLGA@BP-R848+DC-mGPC3pp + NIR group was superior to that of the DC-mGPC3pp group. It was observed that the single photothermal therapy yielded superior therapeutic outcomes for solid tumors when compared to immunotherapy alone. Approximately 10 days later, the tumor growth in the PLGA@BP-R848+NIR group gradually resumed, suggesting that photothermal therapy by itself cannot generate immunity and prevent tumour recurrence. Importantly, the PLGA@BP-R848+DC-mGPC3pp + NIR group showed the highest tumor growth inhibition compared to the other groups, with all 5 mice in this group showing tumor suppression and no recurrence, while the tumor completely disappeared in 3 mice, indicating a significant combined PTT with immunotherapy significantly enhances the therapeutic effect (Fig. 7B–C). No significant side effects, including abnormal weight loss and dietary or activity disorders, were observed in any of the groups.

Next, the anti-tumor immune response of the mice was explored by detecting the infiltration of CTLs (CD3<sup>+</sup> CD8<sup>+</sup> IFN- $\gamma$ +), helper T cells (CD3<sup>+</sup> CD4<sup>+</sup> IFN- $\gamma$ +), and Tregs (CD4<sup>+</sup> CD25<sup>+</sup> Foxp3<sup>+</sup>) at the primary tumor site. The results showed that PLGA@BP-R848+DC-mGPC3pp + NIR significantly enhanced the recruitment of CTLs and helper T cells to the primary tumor, at a rate of 13.60% and 7.20% respectively, which were superior to the effect of PLGA@BP-R848+NIR treatment (6.86% and 3.64%) and single DC-mGPC3pp immune cell therapy (3.13% and 1.64%). In contrast, the control group had only 1.42% and 1.17% infiltration of lymphocytes (CD4<sup>+</sup> IFN- $\gamma$ + and CD8<sup>+</sup> IFN- $\gamma$ +) into the tumor (Fig. 7D). In addition, the combination therapy group exhibited a remarkable decrease in

the proportion of intratumoral Tregs (0.79% vs 7.72% in Control group, 4.27% in DC-mGPC3pp group, and 1.68% in PLGA@BP-R848+NIR group) compared to the control group and the two single therapy groups. These findings suggested that PTT combined with DC immunotherapy enhanced the antitumor immune response by generating potent lymphocyte-mediated killing of tumor cells and inhibiting the intratumoral infiltration of Tregs. Further statistical analysis confirmed the infiltration of the immune cells CTLs, helper T cells, and Tregs, by PLGA@BP-R848+NIR in the primary tumor (Fig. 7D–E). Further analysis of the tumor microenvironment was performed using multiple immunofluorescence staining. The results revealed that in mice treated with PLGA@BP-R848 combined with DC immunotherapy and photothermal therapy (PTT), there were numerous and large infiltrated lymphocyte clusters within the tumor. It was observed that lymphocytes infiltrated the tumor, forming TLS with a significant number of B cells surrounding T cells (Fig. 7F). Hence, the photothermal burst accompanied by R848 and GPC3-specific DC vaccine enhanced the antitumor immunity of CTLs and helper T cells, simultaneously reduced the immunosuppressive activity of Tregs, and facilitated the formation of TLS, resulting in a remarkable synergistic antitumor effect.

#### 4. Discussions

Most cancer vaccines currently under development are associated with known tumor antigens rather than all antigens associated with tumor cells, leading to insufficient tumor antigen recognition. Additionally, the dysfunction of immune cells in the tumor microenvironment and the lack of infiltrating lymphocytes greatly impact the effectiveness of immunotherapy [1,2,29,30]. This study described the use of nano-immunoadjuvants combined with black phosphorus nanosheets to produce the photothermal effect for tumor ablation. PLGA@BP-R848 NPs, constructed by encapsulating biodegradable and biocompatible multifunctional nano-materials, possess unique immune-regulating properties and high photothermal effect, facilitating the efficient eradication of primary tumors and enhancement of anti-tumor immune therapy. Importantly, PLGA@BP-R848 NPs exhibited good targeting and photothermal efficacy. Under near-infrared light, locally administered PLGA@BP-R848 NPs generate photothermal killing of the majority of tumor cells and release BP and the drug R848. On one hand, the release of BP triggers programmed cell death of remaining cancer cells through the mitochondrial pathway; on the other hand, the tumor antigens generated by the photothermal effect exhibit a synergistic effect when combined with the TOLL-like 7/8 receptor agonist R848 in immune cell DC therapy. This combination activates the anti-tumor immune response, promoting infiltration of immune cells and facilitating the eradication of residual tumor cells. To investigate its anti-cancer effect, in a mouse model of liver cancer, PLGA@BP-R848 NPs combined with immune cell therapy significantly suppressed local tumor growth, accompanied by a significant decrease in immunoregulatory cells Treg and an increase in infiltration of CD8<sup>+</sup> and CD4<sup>+</sup> T cells, resulting in an anti-tumor effect. Therefore, our study proposes a strategy for the treatment of cancer using nano-immunoadjuvants combined with photothermal effect, which can eliminate primary tumors, kill residual tumor cells, and improve anti-tumor immunity.

The anti-tumor efficacy of tumor immunotherapy is limited by the strict physical barrier of tumors and the low infiltration efficiency of immune cells [3]. T lymphocytes within the tumor, through their cytotoxic function, play the most important role in anti-tumor activity [31]. The increase in infiltrating T cells (CD8<sup>+</sup> and CD4<sup>+</sup> T cells) in the tumor microenvironment is associated with improved prognosis in liver cancer [32,33]. PLGA@BP-R848 NPs can induce ICD and release tumor antigens through PTT, while R848, a synthetic Toll-like receptor 7 and 8 agonist, elicits both innate and adaptive immune reactions and boosts T cell cytotoxicity to overcome this obstacle. In vitro cell experiments have shown that PLGA@BP-R848 NPs, after generating photothermal effects, activate the mitochondrial apoptotic pathway Bcl-2-Bax-Cytochrome c-caspase-3 and inhibit the PI3K-AKT-mTOR signaling pathway for cell growth. Our findings align with the investigations conducted by Shang Y and Wu Q et al. [34,35]. Dead tumor cells can reactivate immune cells as novel antigens and initiate local inflammation, facilitating the migration of T-cells into the tumor, thereby enhancing the immune response against the tumor. Experiments utilizing a mouse liver cancer model have evidenced that PLGA@BP-R848 NPs combined with NIR can activate immune cells in the mouse spleen, notably increase the proportion of CD8<sup>+</sup> T cells, prompt a systemic anti-tumor immune response, completely eradicate the primary tumor, and effectively suppress tumor recurrence and metastasis.

It is noteworthy that BP, as a PTT driver for tumor immunogenicity, synergizes with the immune adjuvant R848 to enhance tumor immune strengthening and improve the efficacy of immunotherapy. In addition, the combination of PLGA@BP-R848 NPs with DC immune cells effectively stimulate the migration of effector T cells into "cold" tumors and reduce the suppressive effect of regulatory T cells, and facilitate the formation of tertiary lymphatic structures (TLS), thus improving the immunosuppressive microenvironment caused by the tumor and generating a strong anti-tumor immune response. Lots of studies has revealed that the presence of tertiary lymphoid structures (TLS) in tumors correlates with improved prognosis and also enhances the response to immunotherapy [36–38]. TLS may emerge as an attractive therapeutic target. The shell of PLGA@BP-R848 NPs is comprised of FDA-approved PLGA, while the core BP ultimately degrades into phosphate ions to provide nourishment, and R848 acts as an immune stimulant. Their biotoxicity is negligible *in vivo*, and near-infrared laser irradiation allows for controlled release of PLGA@BP-R848 NPs in tumor tissues, ensuring biocompatibility. Moreover, the platform technology reported here may reduce the side effects of cancer treatment as it is localized, prompting further evaluation for clinical translation. The photosensitive nanoadjuvant PLGA@BP-R848 is closely associated with the Bcl-2-Bax-Cytochrome c-caspase-3 and PI3K-AKT-mTOR signaling pathways; however, the specific mechanisms of their immunostimulatory effects in innate immune cells (e.g., interactions with various signaling pattern-recognition receptors) are still unclear. In a mouse model of hepatocellular carcinoma, PLGA@BP-R848 in combination with DC cell immunotherapy enhanced the effects of DC cell therapy, if combination therapy consisting of PLGA@BP-R848 and other therapies, such as combinations with immune checkpoint-blocking (ICB) drugs, e.g., CTLA-4 and PD-1/PD-L1-blocking drugs, may result in synergistic anti-tumor effects due to the multifaceted anti-tumor mechanisms, which may produce synergistic anticancer effects, need to be further investigated. Moreover, PLGA@BP-R848 NPs to DC immune cells could facilitate the formation of tertiary lymphoid structures (TLS), so our next plan will be to

further investigate the specific mechanism of PLGA@BP-R848 NPs to promote the formation of TLS.

## 5. Conclusions

Our study focuses on the design of photothermal nanoadjuvant PLGA@BP-R848 NPs, which can induce tumor apoptosis via the mitochondrial apoptotic pathway Bcl-2-Bax-Cytochrome c-caspase-3. Moreover, these NPs have the potential to inhibit the PI3K-AKT-mTOR signaling pathway, which plays a crucial role in cell growth and survival. This process enhances the antitumor immune response by promoting the migration and infiltration of immune cells as well as the formation of tertiary lymphoid structures (TLS). Therefore, our study proposes a novel cancer treatment strategy that targets primary tumors, eliminates residual tumor cells, and enhances the anti-tumor immunity to prevent tumor recurrence.

## Ethics statement

All animal experiments in this study were approved by the Experimental Animal Ethics Committee of Jinan University (Guangdong, China). Ethics Committee No. (LL-KY-2020327)

## Consent for publication

Written informed consent was obtained from all the authors for the study.

## Availability of data and materials

The authors declare that all data supporting the results in this study are available in the paper and Supplementary Materials. Source data are available from the corresponding authors upon reasonable request.

## CRedit authorship contribution statement

**Ke Liao:** Writing – review & editing, Writing – original draft, Visualization, Validation, Software, Resources, Data curation, Conceptualization. **Shang Chen:** Project administration, Investigation, Funding acquisition. **Gun Yang:** Resources, Project administration. **Xin Huang:** Project administration, Methodology. **Tianyuan Wang:** Software, Investigation. **Shoubin Long:** Writing – original draft, Software. **Jing Wang:** Visualization, Validation. **Lei Yin:** Methodology, Investigation. **Qingshuang Zou:** Writing – review & editing, Writing – original draft, Supervision, Conceptualization. **Quan Liu:** Writing – review & editing, Visualization, Validation. **Zifen Guo:** Visualization, Validation, Supervision, Software, Resources.

## Declaration of competing interest

The authors declare that they have no known competing financial interests or personal relationships that could have appeared to influence the work reported in this paper.

## Acknowledgements

This study was financially supported by the General Projects of National Natural Science Foundation of China (Nos. 82273236 and 82272779), National Science Fund for Young Scholars (No. 82003036), Shenzhen Nanshan District Science and Technology Project (Nos. NSZD2023038 and NSZD2023013), Guangdong Basic and Applied Basic Research Fund Enterprise Joint Fund (No. 2022A1515220042), National Natural Science Foundation of Shenzhen (No. JCYJ20220530141609021), Daan Gene Crosswise Project (No. HXKY2022002), Shenzhen Nanshan District Newly Introduced Discipline Leader Fund Project (No. NSZD2023020) and 2023 International Science and Technology Independent Cooperation Project (No. GJHZ20220913144213025). We also thank the Instrument Analysis Center of Shenzhen University (Xili Campus) for providing instrumental support for this experiment.

## Appendix A. Supplementary data

Supplementary data to this article can be found online at doi:mmdoio

## Abbreviations

|         |                             |
|---------|-----------------------------|
| AFM     | atomic force microscopy     |
| BP      | black phosphorus            |
| DCs     | dendritic cells             |
| H&E     | hematoxylin and eosin       |
| ICD     | immunogenic cell death      |
| mGPC3pp | mouse-derived GPC3 peptides |

|      |                                  |
|------|----------------------------------|
| NIR  | near-infrared light              |
| NPs  | nanoparticles                    |
| PLGA | poly-(lactic-co-glycolic acid)   |
| PTT  | photothermal therapy             |
| R848 | Resiquimod                       |
| TEM  | transmission electron microscopy |
| TLS  | Tertiary lymphoid structures     |
| TME  | tumor microenvironment           |

## References

- [1] Y. Dotsu, D. Muraoka, N. Ogo, et al., Chemical augmentation of mitochondrial electron transport chains tunes T cell activation threshold in tumors, *J Immunother Cancer* 10 (2) (2022).
- [2] Y.J. Xie, M. Dougan, N. Jailkhani, et al., Nanobody-based CAR T cells that target the tumor microenvironment inhibit the growth of solid tumors in immunocompetent mice, *Proc Natl Acad Sci U S A* 116 (16) (2019) 7624–7631.
- [3] K. Nakamura, M.J. Smyth, Myeloid immunosuppression and immune checkpoints in the tumor microenvironment, *Cell. Mol. Immunol.* 17 (1) (2020) 1–12.
- [4] L. Jenkins, U. Jungwirth, A. Avgustinova, et al., Cancer-associated fibroblasts suppress CD8+ T-cell infiltration and confer resistance to immune-checkpoint blockade, *Cancer Res.* 82 (16) (2022) 2904–2917.
- [5] K. Suresh, J. Naidoo, C.T. Lin, et al., Immune checkpoint immunotherapy for non-small cell lung cancer: benefits and pulmonary toxicities, *Chest* 154 (6) (2018) 1416–1423.
- [6] Y. Liu, Y. Fang, X. Chen, et al., Gasdermin E-mediated target cell pyroptosis by CAR T cells triggers cytokine release syndrome, *Sci Immunol* 5 (43) (2020).
- [7] Y. Zhang, Z. Zhang, The history and advances in cancer immunotherapy: understanding the characteristics of tumor-infiltrating immune cells and their therapeutic implications, *Cell. Mol. Immunol.* 17 (8) (2020) 807–821.
- [8] T. Sun, Y.S. Zhang, B. Pang, et al., Engineered nanoparticles for drug delivery in cancer therapy, *Angew Chem. Int. Ed. Engl.* 53 (46) (2014) 12320–12364.
- [9] D. Yadav, M. Kwak, P.S. Chauhan, et al., Cancer immunotherapy by immune checkpoint blockade and its advanced application using bio-nanomaterials, *Semin. Cancer Biol.* 86 (Pt 2) (2022) 909–922.
- [10] W. Zeng, Z. Li, Q. Huang, et al., Multifunctional mesoporous polydopamine-based systematic delivery of STING agonist for enhanced synergistic photothermal-immunotherapy, *Adv. Funct. Mater.* (2023) 2307241 n/a(n/a).
- [11] Q. Liu, L. Yang, L. Wang, et al., An injectable hydrogel based on Bi(2)Se(3) nanosheets and hyaluronic acid for chemo-photothermal synergistic therapy, *Int. J. Biol. Macromol.* (2023) 125064, 244.
- [12] P. Sun, Z. Li, D. Zhang, et al., Multifunctional biodegradable nanoplastin based on oxaliplatin prodrug cross-linked mesoporous polydopamine for enhancing cancer synergic therapy, *Chin. Chem. Lett.* 35 (1) (2024) 108346.
- [13] M. Tavakkoli Yaraki, B. Liu, Y.N. Tan, Emerging strategies in enhancing singlet oxygen generation of nano-photosensitizers toward advanced phototherapy, *Nano-Micro Lett.* 14 (1) (2022) 123.
- [14] X. Huang, Y. Lu, M. Guo, et al., Recent strategies for nano-based PTT combined with immunotherapy: from a biomaterial point of view, *Theranostics* 11 (15) (2021) 7546–7569.
- [15] J. Yan, C. Wang, X. Jiang, et al., Application of phototherapeutic-based nanoparticles in colorectal cancer, *Int. J. Biol. Sci.* 17 (5) (2021) 1361–1381.
- [16] D. Jana, S. Jia, A.K. Bindra, et al., Clearable black phosphorus nanoconjugate for targeted cancer phototheranostics, *ACS Appl. Mater. Interfaces* 12 (16) (2020) 18342–18351.
- [17] Z. Li, Y. Yu, W. Zeng, et al., Mussel-inspired ligand clicking and ion coordination on 2D black phosphorus for cancer multimodal imaging and therapy, *Small* 18 (26) (2022) e2201803.
- [18] L. He, J. Zhao, H. Li, et al., Metabolic reprogramming of NK cells by black phosphorus quantum dots potentiates cancer immunotherapy, *Adv. Sci.* 10 (8) (2023) e2202519.
- [19] G. Peng, B. Fadeel, Understanding the bidirectional interactions between two-dimensional materials, microorganisms, and the immune system, *Adv. Drug Deliv. Rev.* 188 (2022) 114422.
- [20] C. Wang, X. Ye, Y. Zhao, et al., Cryogenic 3D printing of porous scaffolds for in situ delivery of 2D black phosphorus nanosheets, doxorubicin hydrochloride and osteogenic peptide for treating tumor resection-induced bone defects, *Biofabrication* 12 (3) (2020) 035004.
- [21] K.A. Michaelis, M.A. Norgard, X. Zhu, et al., The TLR7/8 agonist R848 remodels tumor and host responses to promote survival in pancreatic cancer, *Nat. Commun.* 10 (1) (2019) 4682.
- [22] Q. Liu, T. Fan, Y. Zheng, et al., Immunogenic exosome-encapsulated black phosphorus nanoparticles as an effective anticancer photo-nanovaccine, *Nanoscale* 12 (38) (2020) 19939–19952.
- [23] J.S. Harrington, S.W. Rytter, M. Plataki, et al., Mitochondria in health, disease, and aging, *Physiol. Rev.* 103 (4) (2023) 2349–2422.
- [24] E. Vringer, S.W.G. Tait, Mitochondria and cell death-associated inflammation, *Cell Death Differ.* 30 (2) (2023) 304–312.
- [25] J.M. Winter, T. Yadav, J. Rutter, Stressed to death: mitochondrial stress responses connect respiration and apoptosis in cancer, *Mol Cell* 82 (18) (2022) 3321–3332.
- [26] A.S. Alzahrani, PI3K/Akt/mTOR inhibitors in cancer: at the bench and bedside, *Semin. Cancer Biol.* 59 (2019) 125–132.
- [27] H. Jaeschke, M.R. McGill, A. Ramachandran, Oxidant stress, mitochondria, and cell death mechanisms in drug-induced liver injury: lessons learned from acetaminophen hepatotoxicity, *Drug Metab. Rev.* 44 (1) (2012) 88–106.
- [28] C. Gao, Q. Wang, J. Li, et al., In vivo hitchhiking of immune cells by intracellular self-assembly of bacteria-mimetic nanomedicine for targeted therapy of melanoma, *Sci. Adv.* 8 (19) (2022) eabn1805.
- [29] H. Sultan, J. Wu, V.I. Fesenkova, et al., Poly-IC enhances the effectiveness of cancer immunotherapy by promoting T cell tumor infiltration, *J Immunother Cancer* 8 (2) (2020).
- [30] K. Shah, A. Al-Haidari, J. Sun, et al., T cell receptor (TCR) signaling in health and disease, *Signal Transduct Target Ther* 6 (1) (2021) 412.
- [31] L. Gao, C. Zhang, D. Gao, et al., Enhanced anti-tumor efficacy through a combination of integrin alphavbeta6-targeted photodynamic therapy and immune checkpoint inhibition, *Theranostics* 6 (5) (2016) 627–637.
- [32] B. Zhou, J. Yan, L. Guo, et al., Hepatoma cell-intrinsic TLR9 activation induces immune escape through PD-L1 upregulation in hepatocellular carcinoma, *Theranostics* 10 (14) (2020) 6530–6543.
- [33] Y.F. Wang, S.X. Yuan, H. Jiang, et al., Spatial maps of hepatocellular carcinoma transcriptomes reveal spatial expression patterns in tumor immune microenvironment, *Theranostics* 12 (9) (2022) 4163–4180.
- [34] Y. Shang, Q. Wang, B. Wu, et al., Platelet-membrane-camouflaged black phosphorus quantum dots enhance anticancer effect mediated by apoptosis and autophagy, *ACS Appl. Mater. Interfaces* 11 (31) (2019) 28254–28266.
- [35] Q. Wu, Q. Ma, J. Ma, et al., Cascade amplification of pyroptosis and apoptosis for cancer therapy through a black phosphorous-doped thermosensitive hydrogel, *Pharmaceutics* 15 (7) (2023).

- [36] N. Horeweg, H.H. Workel, D. Loiero, et al., Tertiary lymphoid structures critical for prognosis in endometrial cancer patients, *Nat. Commun.* 13 (1) (2022) 1373.
- [37] M. Meylan, F. Petitprez, E. Becht, et al., Tertiary lymphoid structures generate and propagate anti-tumor antibody-producing plasma cells in renal cell cancer, *Immunity* 55 (3) (2022) 527–541 e525.
- [38] W.H. Fridman, M. Meylan, F. Petitprez, et al., B cells and tertiary lymphoid structures as determinants of tumour immune contexture and clinical outcome, *Nat. Rev. Clin. Oncol.* 19 (7) (2022) 441–457.

**Ke Liao**- Institute of Pharmacy and Pharmacology, School of Pharmaceutical Science, Hengyang Medical School, University of South China, Hengyang, Hunan, 421001, P. R. China; Department of Laboratory Medicine, Huazhong University of Science and Technology Union Shenzhen Hospital (Nanshan Hospital), Shenzhen University, Shenzhen, 518052, P. R. China.

**Shang Chen**- Department of Laboratory Medicine, Huazhong University of Science and Technology Union Shenzhen Hospital (Nanshan Hospital), Shenzhen University, Shenzhen, 518052, P. R. China;

**Gun Yang**- Institute of Pharmacy and Pharmacology, School of Pharmaceutical Science, Hengyang Medical School, University of South China, Hengyang, Hunan, 421001, P. R. China; Department of Laboratory Medicine, Huazhong University of Science and Technology Union Shenzhen Hospital (Nanshan Hospital), Shenzhen University, Shenzhen, 518052, P. R. China.

**Xin Huang**- Department of Laboratory Medicine, Huazhong University of Science and Technology Union Shenzhen Hospital (Nanshan Hospital), Shenzhen University, Shenzhen, 518052, P. R. China; Department of Thoracic Surgery, First Affiliated Hospital of Anhui Medical University, Hefei 230032, P. R. China.

**Tianyuan Wang**- Department of Laboratory Medicine, Huazhong University of Science and Technology Union Shenzhen Hospital (Nanshan Hospital), Shenzhen University, Shenzhen, 518052, P. R. China.

**Shoubin Long**- Department of Laboratory Medicine, Huazhong University of Science and Technology Union Shenzhen Hospital (Nanshan Hospital), Shenzhen University, Shenzhen, 518052, P. R. China.

**Jing Wang**- Department of Laboratory Medicine, Huazhong University of Science and Technology Union Shenzhen Hospital (Nanshan Hospital), Shenzhen University, Shenzhen, 518052, P. R. China.

**Lei Yin**- Department of Laboratory Medicine, Huazhong University of Science and Technology Union Shenzhen Hospital (Nanshan Hospital),

**Qingshuang Zou**- Department of Chemistry, The Chinese University of Hong Kong, Shatin, N.T., Hong Kong, 999077, P. R. China.

**Quan Liu**- Department of Laboratory Medicine, Huazhong University of Science and Technology Union Shenzhen Hospital (Nanshan Hospital), Shenzhen University, Shenzhen, 518052, P. R. China; Division of Hepatobiliary and Pancreas Surgery, Department of General Surgery, Shenzhen People's Hospital (The Second Clinical Medical College, Jinan University), Shenzhen 518020, P. R. China.